I Three-Dimensional Average-Shape Atlas of the Honeybee Brain and Its Applications

Abstract

The anatomical substrates of neural nets are usually composed from reconstructions of neurons that were stained in different preparations. Realistic models of the structural relationships between neurons require a common framework. Here we present 3-D reconstructions of single projection neurons (PN) connecting the antennal lobe (AL) with the mushroom body (MB) and lateral horn, groups of intrinsic mushroom body neurons (type 5 Kenyon cells), and a single mushroom body extrinsic neuron (PE1), aiming to compose components of the olfactory pathway in the honeybee. To do so, we constructed a digital standard atlas of the bee brain. The standard atlas was created as an average-shape atlas of 22 neuropils, calculated from 20 individual immunostained whole-mount bee brains. After correction for global size and positioning differences by repeatedly applying an intensity-based nonrigid registration algorithm, a sequence of average label images was created. The results were qualitatively evaluated by generating average gray-value images corresponding to the average label images and judging the level of detail within the labeled regions. We found that the first affine registration step in the sequence results in a blurred image because of considerable local shape differences. However, already the first nonrigid iteration in the sequence corrected for most of the shape differences among individuals, resulting in images rich in internal detail. A second iteration improved on that somewhat and was selected as the

standard. Registering neurons from different preparations into the standard atlas reveals 1) that the m-ACT neuron occupies the entire glomerulus (cortex and core) and overlaps with a local interneuron in the cortical layer; 2) that, in the MB calyces and the lateral horn of the protocerebral lobe, the axon terminals of two identified m-ACT neurons arborize in separate but close areas of the neuropil; and 3) that MB-intrinsic clawed Kenyon cells (type 5), with somata outside the calycal cups, project to the peduncle and lobe output system of the MB and contact (proximate) the dendritic tree of the PE1 neuron at the base of the vertical lobe. Thus the standard atlas and the procedures applied for registration serve the function of creating realistic neuroanatomical models of parts of a neural net. The Honeybee Standard Brain is accessible at `http://www.neurobiologie.fu-berlin.de/beebrain`.

Introduction

Neuronal circuits are composed of multiple neurons wired in a particular fashion for local computation of the information flow in the nervous system. The analysis of the structure of neural nets requires the selective staining of the participating neurons, their three-dimensional (3-D) reconstruction, and composition of these reconstructions into a common frame. Staining of the participating neurons is performed in separate preparations, and, even when double or triple stainings were performed in one brain, a whole network can only be composed from the data collected from numerous preparations. An ideal frame for the precise composition of multiple reconstructions would be an atlas of the brain that contains a large number of landmarks for registering different brains into one reference. We critically tested the suitability of this approach by creating a standard atlas of the bee brain and filling in marked neurons of the olfactory pathway collected from multiple honeybee brains. We find that our standard atlas can indeed be successfully used to construct com-

ponents of a neural net from separately acquired neurons with precise spatial relations. Neuroanatomical atlases of the brain, very much like their geographical analogues, are spatial reference maps that present the multiple functional and structural properties of the nervous system in a common spatial framework. Unlike geographical features, however, anatomical objects such as the brain exist in countless instances, no two of them being actually identical. Although individual brains of a particular species are thought to resemble each other widely, we know that brains, as with the subjects they belong to, differ in size and shape. Therefore, it is desirable that any anatomical brain atlas be representative or average with respect to size and shape. Recent advances in 3-D imaging techniques, image analysis algorithms, and computer hardware have leveraged the creation of digital brain atlases for a number of different animal species (for reviews see Toga and Thompson, 2001;Van Essen, 2002; mouse: Dhenain et al., 2001; zebrafish: Isogai et al., 2001; macaque: Martin and Bowden, 2000; baboon: Black et al., 2001). For invertebrates, a population-based quantitative atlas of the fruit fly *Drosophila melanogaster* has been presented by Rein et al. (2002); see also `http://flybrain.uni-freiburg.de/flybrain` and `http://www.neurofly.de`. The honeybee, *Apis mellifera*, has been studied extensively with respect to its sensory and neural capacities in navigation, communication, visual and olfactory learning, and memory processing (Von Frisch, 1967; Menzel et al., 1996; Menzel, 1999; citealpmenzel2001). The worker honeybee brain contains approximately $8.2 \cdot 10^5$ neurons and is smaller than 1 mm^3 (Witthoeft, 1967), and its overall structure is rather well known (for review see Mobbs, 1985). Furthermore, it offers relatively easy and direct access to the electrophysiology of single-marked cells (Mauelshagen, 1993; Rybak and Menzel, 1998; Abel et al., 2001) and optical recording of single or populations of neurons (Galizia and Menzel, 2000). Although honeybee brain structures are well established, with the first accounts dating back to the Nineteenth Century (Dujardin, 1850; Kenyon, 1896 Mobbs,

1982), a 3-D atlas first became possible with the introduction of confocal microscopy. This method allows the acquisition of optical cross-sections from fluorescently stained specimens with the resolution of light microscopy, without physically sectioning the specimen. Modern functional imaging techniques, as well as new advanced staining methods, have therefore called for a versatile and standardized spatial reference of the whole honeybee brain. We decided to create an average bee brain atlas rather then using a representative brain as an atlas. Transforming an image to match another image, in a way that anatomically maps corresponding points in the two images onto each other, is commonly referred to as registration (Ashburner and Friston, 1999). Because of differences in shape, i.e., differences that cannot be accounted for by an affine transformation (translation, rotation, anisotropic scaling, and shearing), so-called nonrigid or elastic registrations have to be employed.

The averaging method applied here is based on ideas by Ashburner (2000) and Guimond et al. (2000), which finds an average shape image through an iteration of one affine registration, followed by multiple nonrigid registrations (Rohlfing et al., 2001; Rohlfing et al., 2004). The central idea of this method is to first register all images to an (arbitrarily chosen) initial reference using affine registration, create an initial average image, then register all images nonrigidly to this average, generate a new average, and so forth. The underlying idea is that, after several such iterations, the average converges to the shape centroid of the population, which is, up to an affine component (position, orientation, and anisotropic scaling), independent of the choice of the initial reference image (Guimond et al., 2000). The first part of this paper presents neurons of the olfactory pathway collected from different individual brains suitable for registration into the Standard Brain atlas. Then, we evaluate the standard atlas and find that the computed average is indeed a shape centroid of the sample.

A standard brain is of limited value unless it is available to the whole scientific community.

Therefore, the Honeybee Standard Brain atlas can be downloaded from `http://www.neurobiologie.fu-berlin.de/beebrain`.

Material and Methods

Honeybees

Worker bees (*Apis mellifera carnica*) were caught at the hive entrance or in an indoor flight room, immobilized by cooling, and mounted in plastic tubes. The bees were fed with sucrose solution and kept in the dark at 20 °C and high humidity. On the following day, the head was fixed with wax and opened between the median ocellus and the base of the antennae. Glands and tracheal sheaths were removed. A second hole was cut to expose the esophagus. Small droplets of bee physiological saline solution (in mmol[1]: 136 NaCl, 3 KCl, 10 Na_2HPO_4, 2 KH_2PO_4, 105 sucrose, pH 6.7) were applied.

Olfactory interneurons

Intracellular staining Electrodes were pulled with a flaming/brown horizontal puller (Sutter Instruments, Novarto, CA), and their tips were filled with 4 % tetramethylrhodamin-biotin dextran (TMR-Biotin; Micro-Ruby; Molecular Probes, Eugene, OR) or 4 % fluorescein-biotin dextran (FSC-Biotin; Micro-Emerald; Invitrogen, La Jolla, CA) in 0.2 M potassium acetate. The electrode was inserted into the antennal lobe, where recordings from single neurons were performed at different depths. Electrode resistances in the tissue ranged between 140 and 200 M Ω. After the odor stimulation experiment, Micro-Ruby or Micro-Emerald (Molecular Probes) was injected by using depolarizing pulses of 1-2 Hz and 0.2 seconds duration. Complete filling of neurons required dye injection for 30 - 45 minutes.

After intracellular filling, the dye was allowed to diffuse from 3 hours up to overnight. A silver wire placed into the eye served as the indifferent electrode.

Neuropil counterstaining After dissection, the brains were fixed in 4 % formaldehyde diluted in 50 % methanol for 24 hours at 4 °C. Preparations were rinsed for 10 minutes in phosphate-buffered saline (PBS; pH 6.7), diluted 1:4 in distilled water, dehydrated in an increasing ethanol series (30 %, 50 %, 70 %, 90 %, 99 %, 100 %, 10 minutes each), degreased in xylol for 5 minutes, and rehydrated in a decreasing ethanol series. Brains were then washed for 10 minutes in PBS and blocked in 10% normal goat serum (NGS; Sigma, St. Louis, MO) in PBS for 30 minutes at room temperature. Then, the preparations were incubated in the primary antibody SYNORF1 (Klagges et al., 1996), diluted 1:10 in PBS for 48 hours at 4 °C. The primary antibody originates from a screen of Drosophila synapse proteins and was kindly provided by Dr. E. Buchner, (Wuerzburg, Germany). To intensify the intracellular staining of the recorded neuron, streptavidin-Cy3 or streptavidin-Alexa-488 (Invitrogen), diluted 1:500, was added to the primary antiserum. Brains were rinsed in PBS for 15, 30, 45, and 60 minutes and then incubated for 24 hours with a Cy5-conjugated mouse anti-rabbit secondary antibody (Jackson Immunoresearch, West Grove, PA; dilution 1:500 in PBS). After another four rinses in PBS for 15, 30, 45, and 60 minutes, brains were dehydrated in an increasing ethanol series, precleared in a mixture of 30 % methyl-salicylate (MS) and 100 % ethanol, and mounted as whole mounts in MS in double-sided custom slides.

Confocal imaging and reconstruction Wholemount preparations or vibratome sections were imaged with a confocal laser scanning microscope (Leica TCS SP2) with a Leica HC PL Apo $\times 20/0.7$ dry lens objective for the projection neurons (PN) and an HC PL Apo $\times 20/0.7$ CORR/IMM lens for the local interneuron. The local interneuron was imaged in one scan with a voxel size

of $0.42 \times 0.42 \times 1\,\mu$m, whereas, for the PN, 2×2 tiled stacks of 350 optical sections each were scanned with 1024×1024 voxels each and a voxel size of $0.73 \times 0.73 \times 2\,\mu$m. For the PN, either Cy3 was excited by using the 543 nm line of a HeNe laser or Alexa-488 was excited by using the 488 nm line of an ArKr laser, and either of them was scanned as the first channel. Cy5 was excited with the 633 nm line of an HeNe laser and scanned as the second channel. For the reconstruction of the innervated neuropil, the scans of the second channel were resampled to lateral dimensions of 512×512. In the case of tiled images, stacks were combined with the Merge module in Amira. Neuropil outlines were then traced with Amiras segmentation editor. Tracing and reconstruction of the neurons, including topology, lengths, and diameters, were done with a custom module in Amira (Mercury Computer Systems, Inc, San Diego, CA; Schmitt et al., 2004). This module aids the tracing process and creates surface models where neurites are approximated by cylinders of particular length and thickness. In the case of tiled scans (PN), tracing and reconstruction were done on the single tiles and reassembled using the custom module. When vibratome sections were scanned, the images were merged into the standard atlas by using the procedures described below.

Kenyon cells and Pe1 neurons

Staining Kenyon cells were stained by injecting Lucifer yellow (Sigma) iontophoretically into the mushroom bodies (MB) with the neuropil injection technique described by Rybak and Menzel (1993). The electrode was inserted into the ventral vertical lobe. Depolarizing current pulses of 1 Hz and 0.2 seconds duration were applied with a Grass SD-9 stimulator. Iontophoresis times ranged from 10 to 30 minutes, and the resistance varied between 60 and 200 MΩ. The Pe1 neuron was intracellularly stained as described for the olfactory interneurons; however, no neuropil counterstaining was applied. For the Kenyon cell,

specimen fixation was performed as described above except that 0.1 % glutaraldehyde was added to the primary fixative. After that, a standard histology (dehydration and clearing in MS) was applied to both preparations. For the confocal imaging of the Pe1 neuron, the brain preparation was sectioned parallel to the frontal plane at approximately 200 μm depth by using a vibratome.

Confocal imaging and reconstruction Both Pe1 neuron and Kenyon cells were imaged with the Leica TCS 4D confocal microscope by using either the 476 nm (Kenyon cells) or 568 nm (Pe1) line of its ArKr laser. The Kenyon cells were imaged with a Leica PL Fluotar $\times$ 16 / 0.5 IMM (oil) lens using 512 $\times$ 512 voxels lateral, 1.22 μm per voxel and 120 sections 3.03 μm apart. With the Pe1 preparation, four scans in total were made with this preparation. One was done with a Leica PL Apo $\times$ 20 / 0.6 dry lens on the unsectioned specimen (not shown here). Two scans were made on the sectioned preparation with a Leica HC PL Apo CS $\times$ 20 / 0.7 IMM/CORR lens and oil for immersion. A fourth scan used a $\times$ 50 / 0.9 oil lens. In both preparations, neuropil boundaries were traced with the Amira segmentation editor aided by the weak but nevertheless distinct autofluorescence signal in each preparation.

The standard brain

Histology Twenty adult foraging honeybee workers reared in the laboratory were collected at the hive, immobilized with ice, and decapitated. Head capsules were opened from the anterior in PBS (137 mM NaCl, 2.7 mM KCl, 10.1 mM Na_2HPO_4, 1.8 mM KH_2PO_4), antennae, tracheae, and glands removed, and the mouth parts cut off. Then, heads were prefixated for about 30 minutes in 4 % paraformaldehyde (PFA) to keep tissue distortions at a minimum. Finally, brains were dissected from the head capsule, carefully freed from tracheal and glandular tissue from the posterior, and fixed in 4 % PFA for at least another

1.5 hours. Brains were then rinsed six times for 1 hour each in PBS + 1 % Triton X-100 (PBST), blocked with 10 % NGS in PBST (NGS-PBST) for at least 1 hour, and then incubated for 60 hours in the primary antisera nc46 (Reichmuth et al., 1995) and SYNORF1 each diluted 1:30 in NGS-PBST. The primary antibody nc46 also originates from a screen of Drosophila synapse proteins and was kindly provided by Dr. E. Buchner (Wuerzburg, Germany). Preparations were again rinsed six times for 1 hour each in PBST until they were incubated for 36 hours with a Cy3-conjugated mouse-anti-rabbit secondary antibody (Jackson Immunoresearch; dilution 1:200 in NGS-PBST). After another six rinses in PBS each lasting for 1 hour, brains were dehydrated in an increasing ethanol series (50 %, 70 %, 90 %, 99 %, 2×100 %, 10 minutes each), cleared in MS, and mounted as whole mounts in Permount (Fisher Scientific, Fair Lawn, NJ) in double-sided custom slides.

Confocal microscopy Whole mounts were imaged with a confocal laser scanning microscope (Leica TCS 4D) with a Leica HC PL Apo $\times$ 10 / 0.4 dry lens. The specimen was excited with the 568 nm line of an ArKr laser. The emitted light was detected with a LP590 longpass filter and digitized with eight-bit resolution. Because the size of the dissected and embedded brain (app. $2.5 \times 1.6 \times 0.8$ mm) exceeded the maximal field of view (FOV) in this configuration (1 mm^2), the brains were imaged by using multiple image-stack acquisition (3-D-MISA; Zuschratter et al., 1998). Thereby the entire brain was imaged in 2×3 partially overlapping tiles, each using 512×512 pixels in plane and between 84 and 114 sections axially. Stacks were subsequently combined in custom software or a script running in Amira, a 3-D visualization and data analysis package (Mercury Computer Systems Inc./TGS series; `http://www.mc.com/tgs`). The final image volume contained 84–114 slices with a thickness of 8 μm each. After resampling of the images laterally to half of the original dimensions, each slice had 610–749 pixels in the x direction and 379–496

pixels in the y direction with pixel size of 3.8 μm. Because of the refractive index mismatch in the optical path, dry lenses usually introduce a shortening of distances in the z direction. According to Bucher et al. (2000), shortening can be considered as a linear scaling in the z direction. We estimated the scaling factor from preparations that were scanned with both oil and dry lenses to be 1.6.

Image segmentation and reconstruction Image segmentation was done with Amira on a graphics workstation (SGI O2, R5000, 832 MB RAM) or on a PC (Pentium II, 350 MHz, 256 MB RAM running Linux). In most cases, no image processing was necessary on the raw images, except for an adjustment of the gray-scale window. In some cases, unsharp masking filters were applied to enhance faint contours. Subsequently, stacks were loaded into the Amira segmentation editor, and the neuropil areas of interest were traced manually on each slice. We distinguished 22 major compartments (see Fig. 1, Table 1). Tracing results were stored in separate image volumes, in which each voxel no longer encodes the staining intensity but represents a certain label coding for a particular brain structure. These so-called label fields were used for a morphometric analysis and shape averaging (see below) as well as for the reconstruction of polygonal surface models of the brain structures.

Creating the standard brain

The iterative rigid and nonrigid registration scheme used for averaging is described in detail by Rohlfing et al. (2001). The following paragraphs summarize the main ideas, practically without detailed mathematical formalism. Readers interested in the mathematical and algorithmic background are referred to the original publication.

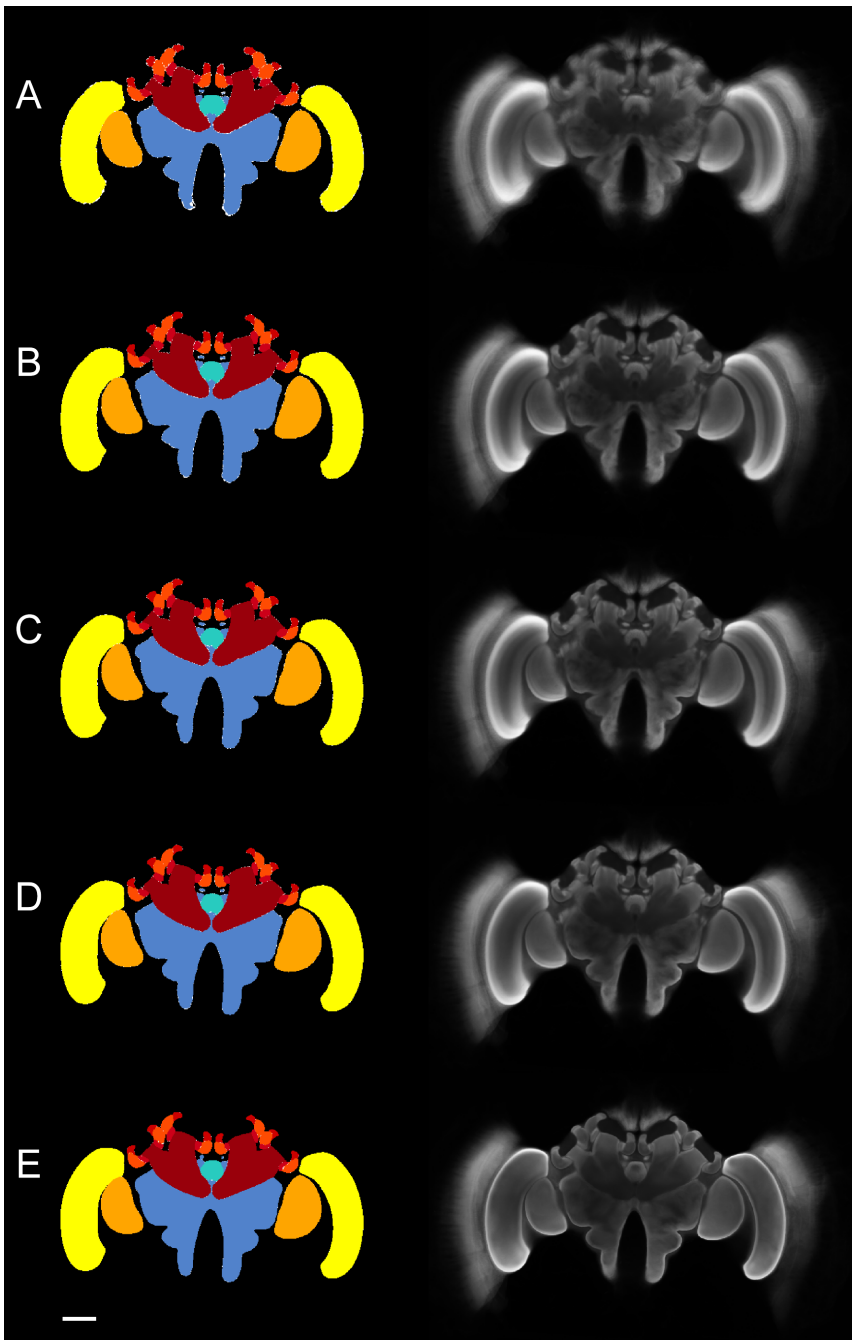

Figure I.1:
A - E: Sequence of average images resulting from the iterative registration procedure. Shown are central axial slices from average label images (left panels) and average gray images (right panels) that were calculated by applying the transformation found for label images to the gray images. After affine registration (**A**) and after first (**B**), after second (**C**), after third (**D**), and after fourth (**E**) nonrigid registration iteration. The colors in the label images correspond to the segmented brain regions (see Fig. 3). White voxels depict undecided voxels, i.e., voxels that could not be assigned to any of the 22 different regions by a simple majority (t = 0 %) threshold. Scale bar = 200 μm in **E** (applies to **A** **E**).

Registration Computing the average of a population of label images first requires accurately mapping corresponding voxels in all images onto each other. For any two images, this mapping is mathematically described by a coordinate transformation, T, that maps the image coordinates of the "floating image" (i.e., the image that is being transformed in space) onto those of the fixed "reference image". The transformation T is usually described by a vector, p, of parameters. Registration can be considered the process of finding p such that some similarity measure computed between the transformed floating image and the reference image is maximized. The intensity-based algorithm used for the average shape atlas utilizes the entropy-based normalized mutual information (NMI; Studholme et al., 1999) image similarity measure to quantify the similarity between the two images. The first step of intersubject registration aims to correct for positioning and global size differences between the individual images, i.e., translation, rotation, and anisotropic scaling (affine registration). Consequently, we initially apply a 9-degree-of-freedom (DOF) affine registration algorithm. Once the images have been normalized to the same affine space, less constrained, nonrigid registration is applied to determine and correct for local shape differences also. Likewise, the nonrigid algorithm determines the set of parameters of a nonrigid transformation T that maximizes the NMI similarity measure. In this step, T is modeled as a cubic B-spline free-form deformation (Sederberg and Parry, 1986) defined on a data-independent, uniformly spaced control point grid covering the reference image. Such a transformation has substantially more DOF than an affine transformation, up to several hundred thousand in our case. The parameters of this nonrigid registration transformation that maximize the NMI similarity measure are determined by appropriate optimization methods (see Rohlfing et al. (2001) and references therein).

Iterative averaging A method for the iterative generation of average images with nonrigid registration was proposed by Ashburner (2000). The central idea

is to first register all original images to a common, arbitrarily chosen reference and then generate an initial average image. Because of the shape differences among different individuals, the initial affine registration will be fairly inaccurate, and the initial average image will thus be blurred. The original images are then registered to the initial average image by using a nonrigid transformation, after which a new (less blurred) average image is generated, and so forth. All iterations except for the first employ nonrigid registration and use the average image resulting from the previous iteration as the reference image, whereas all original individual images are used as floating images. As a result, all floating images are mapped into the same reference space, thus allowing the generation of the next average image.

Label averaging For each iteration, after the transformation of all label images to a common coordinate space, an *average label image* has to be computed. Because labels are nonnumerical data, this average cannot be the arithmetic mean or median. Instead, from the distribution of labels among all corresponding voxels, the label that occurs most frequently is selected and assigned to be the *average label*. In cases where there is no unique most frequent label, the resulting average voxel is assigned the label "undecided." This definition of "average" is commonly referred to as the mode of the label distribution. In addition, we parameterize the mode by requiring the selected label to represent at least t percent of the valid voxels. For $t = 0\%$, this definition is equivalent to the political voting concept known as relative majority (plurality); for $t = 50\,\%$, an absolute majority of labels is required; for $t = 100\,\%$, a unanimous decision is required. Decisions resulting from other values are generically called qualified majorities.

In general, as the value of t increases, the number of voxels that cannot be assigned an unambiguous average label increases as well. Undecided voxels are excluded from the computation of the NMI similarity measure. For the first (affine) iteration, t was set to $0\,\%$ to arrive quickly at a reasonable average

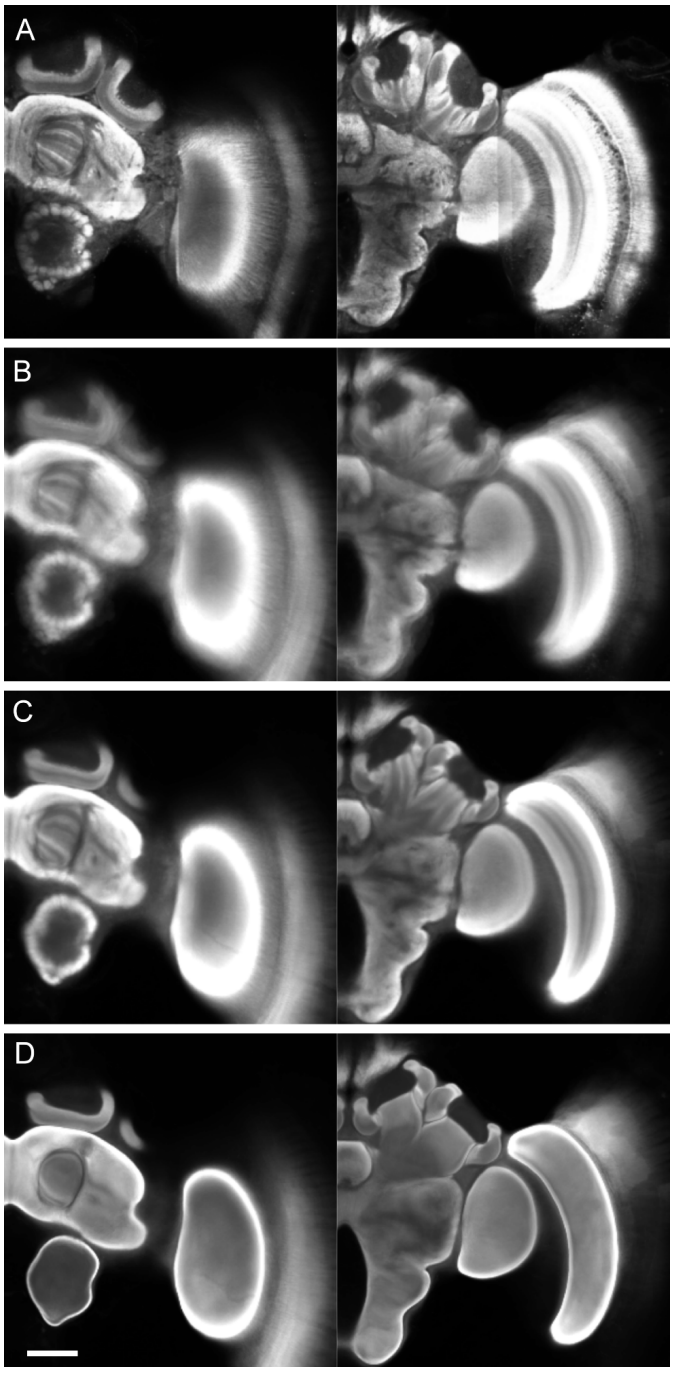

Figure I.2:
Average gray images were used to control for the quality of the averaging process. Label images have no information that could be exploited by the registration algorithm to find the correct transformations inside a labeled structure. If the transformations are correct, then homologous parts in the images are superimposed and lead to a sharpening of those inner structures. If not, details within the labeled regions get smeared. In each panel from **A** to **D** there are two close-ups from the left brain hemisphere at approximately 250 μm (left panels) and 450 μm (right panels) beneath the frontal surface. **A** is taken from the initial template, **B** from the average gray image after affine registration, **C** from the second nonrigid iteration, and **D** from the fourth. Scale bar = 200 μm in **D** (applies to **A** **D**).

image. All subsequent iterations worked with a t = 50 % in order to ensure a high confidence for the average label image.

Figure 1 summarizes the results of the iterative registration. The left panels show central slices of the average label images. The labels corresponding to the different anatomical structures are displayed in different colors, and the regions in which there was no agreement for one of the 22 labels, the so-called undecided voxels, are shown in white. Numerical values for the percentage of undecided voxels are summarized in Table 1. The right panels in Figure 1 show the corresponding average gray images that were generated using the following procedure: The transformation found for each individual label image was applied to the corresponding microscopy image, and the arithmetic mean of the intensity value for all subjects was calculated at each voxel position.

		Nonrigid			
t	Affine	1st	2nd	3rd	4th
0%	3.4	1.4	1.1	0.7	0.3
50%	5.6	1.9	1.5	1.0	0.4
66%	22.2	8.8	7.1	4.8	2.0
100%	77.7	42.1	36.6	25.5	12.6

Table I.1:
Percentages of "Undecided" Voxels in the Average Label Images for Different Averaging Thresholds (The percentages are calculated from the total number of voxels in each average label image, excluding background).

As can be seen in Figure 1 and Table 1, after affine registration, i.e., after correcting for differences in position and size, there is only a fraction of 3.4 % undecided voxels, meaning that more than 96 % of the voxels could be decisively assigned to a particular brain compartment according to the simple majority threshold. However, in looking at the corresponding gray image, it is obvious that neuropil boundaries are somewhat fuzzy, and internal structures such as strata in the peduncle and the superior optical tract (seen as a dark area within the protocerebral lobes) almost disappear. This substantially became different after the first nonrigid iteration shown in Figure 1B. The relative number of un-

decided voxels here is less than half of that in the affine average (1.4 %), and the corresponding gray image begins to display plenty of the detail already seen in the individual image (cf. Fig. 3).

The second nonrigid iteration (Fig. 1C) is then able to reduce the number of undecided voxels by 0.3 points on the percentage score to 1.1 % and generally enhances the sharpness of the neuropil borders in the gray average. However, as seen in some internal structures, a tendency to smear fine details to homogenous regions is observable. For example, the stratification within the medial peduncle visible in Figure 1B becomes a more or less homogeneous region in Figure 1C. This effect, sharpening the neuropil borders while internal structures are smeared, continues progressively through iterations 3 and 4, ending up in an image that is devoid of fine structure (Fig. 1F). Figure 2 again shows this, in greater detail, for three stages of the iterative process. In Figure 2A D, there are two close-ups from the left brain hemisphere at approximately 250 μm (left) and 450 μm (right) below the frontal surface; A is taken from the initial template, B from the average gray image after affine registration, C from the second nonrigid iteration, and D from the fourth.

Fitting of individual neurons into the standard

For each neuron that is to be fitted into the standard atlas, the neuropil outlines have to be segmented. Because a typical neuron staining does not contain enough information about the neuropil boundaries, it is necessary to apply a generic neuropil counterstaining, preferably one with the same antibodies as used for the Standard Brain. The fitting then consists of a registration of the neurons neuropil regions to those of the atlas. Because scans of neurons typically contain only parts of the brain, registration has to be restricted to the corresponding parts in the Honeybee Standard Brain. To do so, in the label image, some regions have to be removed, and / or the volume has to be cropped to

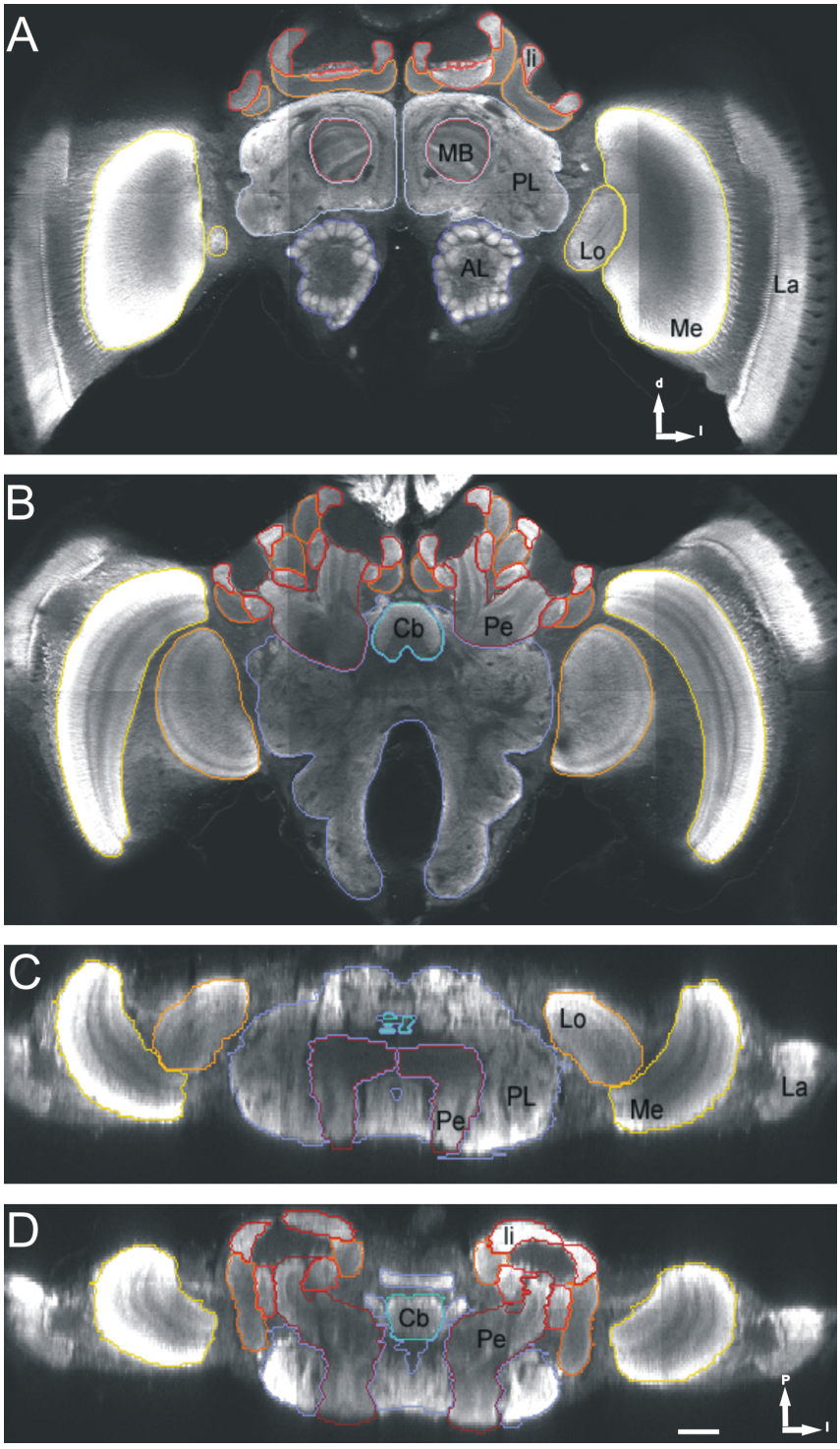

Figure I.3:
Confocal virtual images of an immunostained bee brain. **A:** An axial slice through the honeybee brain at the level of the vertical lobe at approximately 190 μm below the frontal brain surface. **B:** Brain neuropils at the level of the central body (at approximately 300 μm depth). Same orientation as in **A**. **C:** Horizontal slice at approximately 600 μm depth from the top. **D:** Another horizontal section at approximately 360 μm depth from the top. Neuropil regions were manually labelled in all slices by margined colors. Scale bar = 200 μm in **D** (applies to **A** **D**).

fit the field of view of the neuron image. Then, a standard two-step registration is performed consisting of a 9-DOF affine step followed by a nonrigid step. The algorithm used for fitting the neurons for this paper was similar to the one used for generating the average-shape brain atlas.

The main difference is the fact that here we use a custom module within Amira, whereas the iterative averaging used a stand-alone tool by one of the authors. Another difference is that, instead of NMI (normalized mutual information), we use a metric that takes the spatial correspondence of two label fields into account. The result of a registration is a 9-DOF affine transformation matrix and a deformation field (vector field) containing the nonrigid component of the transformation. For fitting the neuron into the atlas, both were applied to the geometric representation of the neuron image.

Structure	Mean Volume [μm^3]	Rel. Volume [%]	SD [μm^3]	Rel. SD [%]	SE [μm^3]	Rel. SE [%]
Protocerebral Lobes and SOG	1.27×10^8	33.36	1.54×10^7	12.08	3.44×10^6	2.70
Central Body	2.32×10^6	0.61	4.10×10^5	17.69	9.17×10^4	3.96
Medulla (l)	5.73×10^7	15.01	8.27×10^6	14.42	1.85×10^6	3.23
Medulla (r)	5.70×10^7	14.92	8.74×10^6	15.34	1.95×10^6	3.43
Lobula (l)	1.66×10^7	4.34	1.95×10^6	11.74	4.35×10^5	2.63
Lobula (r)	1.65×10^7	4.32	1.84×10^6	11.14	4.11×10^5	2.49
Antennal lobe (l)	1.09×10^7	2.85	2.03×10^6	18.62	4.53×10^5	4.16
Antennal lobe (r)	1.08×10^7	2.82	2.01×10^6	18.69	4.49×10^5	4.18
Ventral mushroom body (l)	1.58×10^7	4.15	2.24×10^6	14.12	5.00×10^5	3.16
Ventral mushroom body (r)	1.57×10^7	4.11	1.89×10^6	12.03	4.22×10^5	2.69
Medial basal ring (l)	1.89×10^6	0.50	3.05×10^5	16.10	6.82×10^4	3.60
Medial basal ring (r)	1.90×10^6	0.50	3.05×10^5	16.04	6.83×10^4	3.59
Lateral basal ring (l)	2.09×10^6	0.55	3.42×10^5	16.38	7.65×10^4	3.66
Lateral basal ring (r)	2.02×10^6	0.53	3.49×10^5	17.28	7.81×10^4	3.86
Medial collar (l)	5.97×10^6	1.56	9.78×10^5	16.40	2.19×10^5	3.67
Medial collar (r)	6.00×10^6	1.57	9.37×10^5	15.60	2.09×10^5	3.49
Lateral collar (l)	6.54×10^6	1.71	1.11×10^6	16.98	2.48×10^5	3.80
Lateral collar (r)	6.58×10^6	1.72	1.19×10^6	18.12	2.67×10^5	4.05
Medial lip (l)	4.45×10^6	1.16	8.00×10^5	17.98	1.79×10^5	4.02
Medial lip (r)	4.43×10^6	1.16	7.32×10^5	16.50	1.64×10^5	3.69
Lateral lip (l)	4.76×10^6	1.25	6.84×10^5	14.36	1.53×10^5	3.21
Lateral lip (r)	4.99×10^6	1.31	7.01×10^5	14.05	1.57×10^5	3.14

Table I.2:
Mean Volume, Relative Volume, Standard Deviation (SD), Relative SD, Standard Error (SE), and Relative SE of 22 Segmented Bee Brain Compartments (N=20).

Results

Neuropils composing the honeybee brain

In insects, the lateral protocerebrum consists of the optic lobes, comprising medulla and lobula and the outermost optical layer, the lamina, that underlies the array of retinal photoreceptors. The lamina of the optic lobes was not considered in the Standard Brain. Prominent central brain structures, the MB are enclosed medially and laterally by the protocerebral lobes (PL). The central body (Cb) lies in the median protocerebrum, embedded posteriorly in the PL. The chemosensory system is represented by the antennal lobes (AL) positioned ventrally to the PL. The major outputs of the AL to the central brain are PN targeting the MB and a subcompartment of the PL, the lateral horn (LH). Figure 3A D shows virtual slices through the honeybee brain in orthogonal and horizontal views, depicting the major neuropil areas. As can be seen, the two antibodies (nc46 and SYNORF1) preferentially marked regions with a high synaptic density corresponding to neuropils, whereas somata and tracts were left mostly unstained (Fig. 3A,B). Staining and imaging quality were sufficient to distinguish the major brain compartments. Even sections orthogonal to the plane of image acquisition (Fig. 3C) displayed rich details that could be exploited by the subsequent labeling (see below).

In this study, we focus on the connection in the pathway from the AL to the MB and LH and the output connections of the MB (olfactory pathway). We select three major brain compartments, the innervation of the lip region of the MB calyces and the LH of the PL by olfactory interneurons and the peduncle of the MB, where intrinsic neurons of the MB (Kenyon cells) join with the MB extrinsic neuron PE1.

Labeling and 3-D reconstruction of neuropils and individual neurons

Because different neuropils exhibit similar levels of staining intensity, the gray values in an image cannot be used to specify morphologically coherent subregions. Therefore, each voxel must be labeled as belonging to one of 22 preselected anatomical brain compartments (Table 2). These make up approximately 85 % of the total neuropil. The neuropils not considered were the laminae ganglionares of the optic lobes (Fig. 3B; medulla: yellow; lobula: orange) and the neuropil belonging to the ocelli, including the large fibers descending into the protocerebral lobes (Fig. 3B; blue marginated). When boundaries between functionally or anatomically distinct regions were not reliably visible, they were subsumed into a single label. For example, the peduncle and the vertical and medial lobes of the MB were labeled as ventral mushroom body (Fig. 3B; MB: red), because a precise determination of their boundaries was not possible. Similar procedures were applied to the PL: anatomically distinct regions such as the LH or the optic tubercle are not delimited in the immunostained preparation. Also, the ventral boundary of the PL to the tritocerebrum and subesophageal ganglion was not visible. Therefore, the whole compartment was labeled as protocerebral lobes and subesophageal ganglion. The AL are depicted in Figure 3A in blue. Figure 3C,D shows labeling in two horizontal sections as in Figure 3A,B. We performed a conventional volumetric analysis with the label images of our sample of 20 brains. Table 2 gives means and SD of the absolute and relative volumes of the 22 brain compartments. Relative volumes were obtained by normalizing the volume of a particular structure to the sum of all structures. In addition, polygonal surface models were reconstructed. Such models serve mainly two purposes. First, they can be used to visualize complex anatomical relationships; e.g., semitransparent surface rendering can be used to visualize structures that are enclosed by other structures, structures can be

shown in isolation, and so forth. Second, polygonal models are much smaller than the corresponding label fields or confocal image stacks. Thus, surface models can be used for efficiently reporting anatomical results through the internet. The techniques for recognizing and defining neuropil borders were used in all individual preparations, and this is a prerequisite step to "align" individual neuronal structures to the common framework of the Standard Brain.

Fitting single neurons into the Honeybee Standard Brain

In honeybee neuroanatomy, typical data are single neuron stainings that routinely arise when neurons are recorded intracellularly. The ultimate goal of such experiments is to understand the connectivity between neurons and their relation to neuropils, the final goal being to characterize and identify the anatomical correlates of functional neuronal circuits. Because of interindividual shape differences between brains, this can be achieved only if the brains containing the respective neurons are merged to the same shape. In the following sections, two examples will be presented.

Olfactory interneurons Glomeruli of the AL are separated into core and cortex, with receptor axons from the antenna almost exclusively innervating the cortex (Galizia et al., 1999). Interneurons originating in the Al belong to two main morphological types, the local interneurons (LIN), and the PN running in the antennocerebralis tracts (ACT; Arnold et al., 1985; Fonta et al., 1993; Abel et al., 2001; Mueller et al., 2002). Whereas LIN interconnect olfactory glomeruli, PN relay the processed information to higher order brain centers. Three types of PNs can be distinguished, according to the tract along which their axons run, as medial (m-), lateral (l-), and mediolateral (ml-) ACT neurons. The target areas of the m- and l-ACT neurons are the calyces of the MB and a region in the PL, the LH. Figure 4A,B shows two virtual confocal slices of two different m-ACT

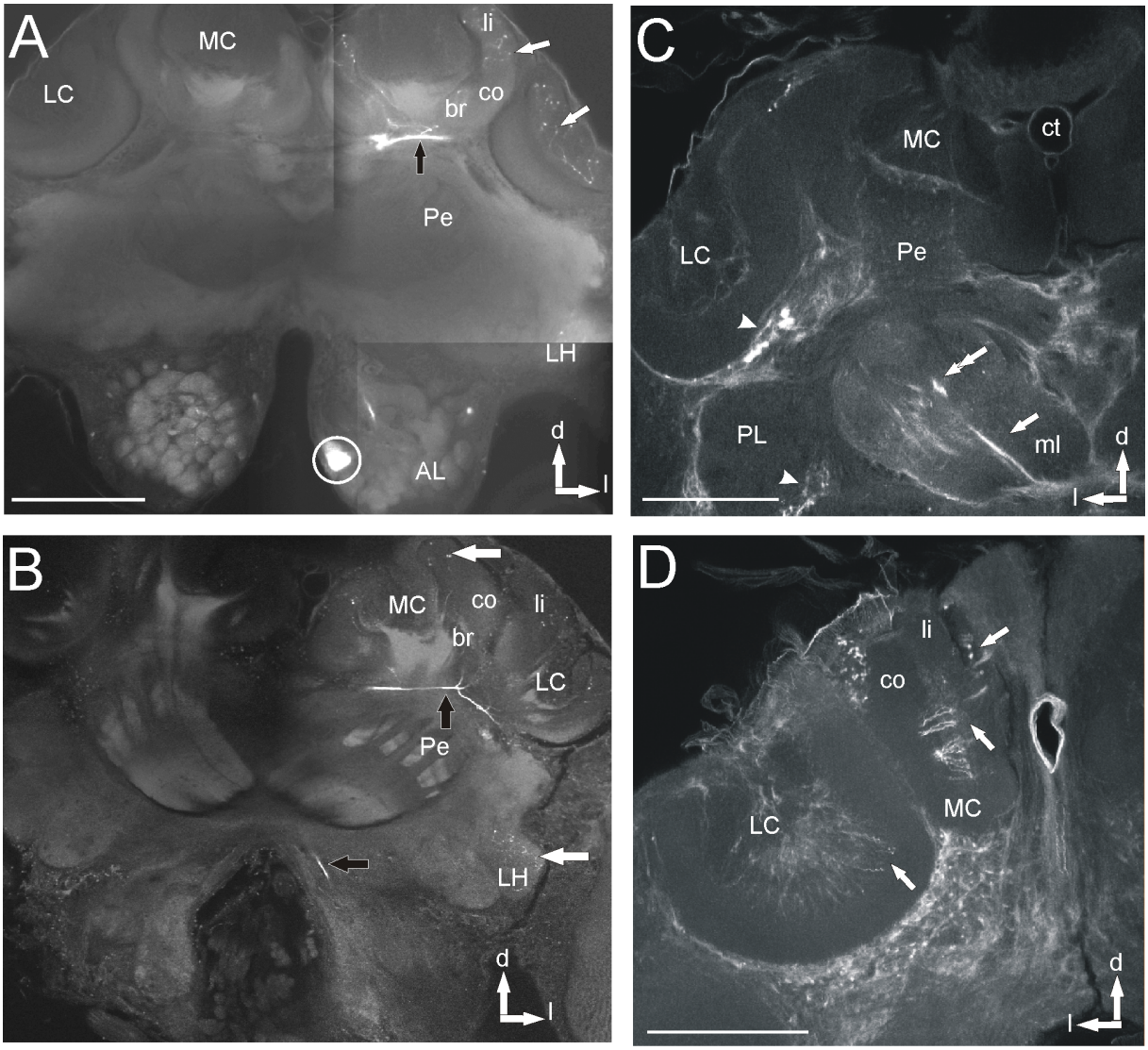

Figure I.4:
Confocal images of projection neurons (PNs) of the median antennocerebralis tract (m-ACT) in two separate preparations at approximately 210 μm depth (**A**) and 230 μm depth (**B**) from the frontal brain surface. **A:** An uniglomerular PN (type I) innervating the glomerulus T3-60 in the antennal lobe (AL; circle). In the protocerebral lobe, its axon branches out (black arrow) and sending collaterals via the inner ring tracts into the MB calyces cups (MC, LC). The main axon descends into the lateral horn (LH). Note the bleb-like structures in the lip region (li; white arrows). **B:** A uniglomerular PN (type II) with the ascending axon more posteriorly in the PL (black arrows). axon terminals are shown in the lip region of the calyces and in the LH (white arrows). **C,D:** The course of clawed Kenyon cells (type K5) in the MB at approximately 250 μm (in **C**) and 500 μm (in **D**) depth from the brain surface. **C:** In the peduncle, K5 axons bifurcate, one strand projecting into the vertical lobe (arrowheads), the other into the medial lobe (ml; white arrows). Arrowheads: Extrinsic neurons of the mushroom bodies. **D:** The clawed Kenyon cell somata are positioned outside the MB calyces cups (MC, LC) and form narrow dendritic trees in these neuropils (white arrows). Scale bars = 200 μm in **A** (applies to **B, C, D**).

neurons intracellularly stained in two preparations (type I in Fig. 4A, type II in Fig. 4B) at depths of 210 μm and 230 μm, respectively, measured from the anterior brain surface. Both neurons have unilateral projections in single but separate glomeruli of the AL (shown for the type I neuron in Fig. 4A, circle). Both m-ACT neurons run through the PL (black arrows in Fig. 4A,B). They give rise to collaterals running via the inner ring tract into the lip region of the MB calyces (Fig. 4B). The axonal terminals form bouton-like structures ("blebs") in the lip region (li) of both calyces and in the LH (white arrows in Fig. 4A,B). In the PL, there is one collateral that bypasses the calyces and proceeds ventrally to the LH (Fig. 4B).

The two m-ACT neurons have been electrophysiologicaly recorded (data not shown here) and intracellularly stained in two different individuals. For each 3-D reconstruction of the neurons the geometric transformation was computed after registration of the respective neuropils to those of the Honeybee Standard Brain. For the PNs, the neuropils that had to be registered were the left AL, the PL, the subesophageal ganglion, and the left MB. Figure 5A,B shows the structural relationship between the two PNs (type I in green and type II in blue). The dendritic field of each the PN arborizes within a single glomerulus.

According to the Antennal Lobe Atlas (Galizia et al., 1999), the glomerulus is identified as T2-04 for the PN depicted in blue and the T3-60 for the PN depicted in green (Fig. 5). Their axons leave the AL medial-dorsally via the m-ACT, passing posteriorly the medial lobes of the MB. In the mediodorsal PL collaterals run via the inner ring tracts of both calyces (Fig. 5B; nine collaterals for the PN depicted in blue and seven collaterals for the PN depicted in green). They continue to the basal ring and then to the lip region of both calyces. There are similar aborization patterns of both PN axon terminals in the lip, including some areas that have no PN terminals (black arrows in Fig. 5C). For better visualization, Figure 5A - C shows only the fine axonal terminals in the frontal half of the lip; both PN also extend their axon collaterals into the posterior half of

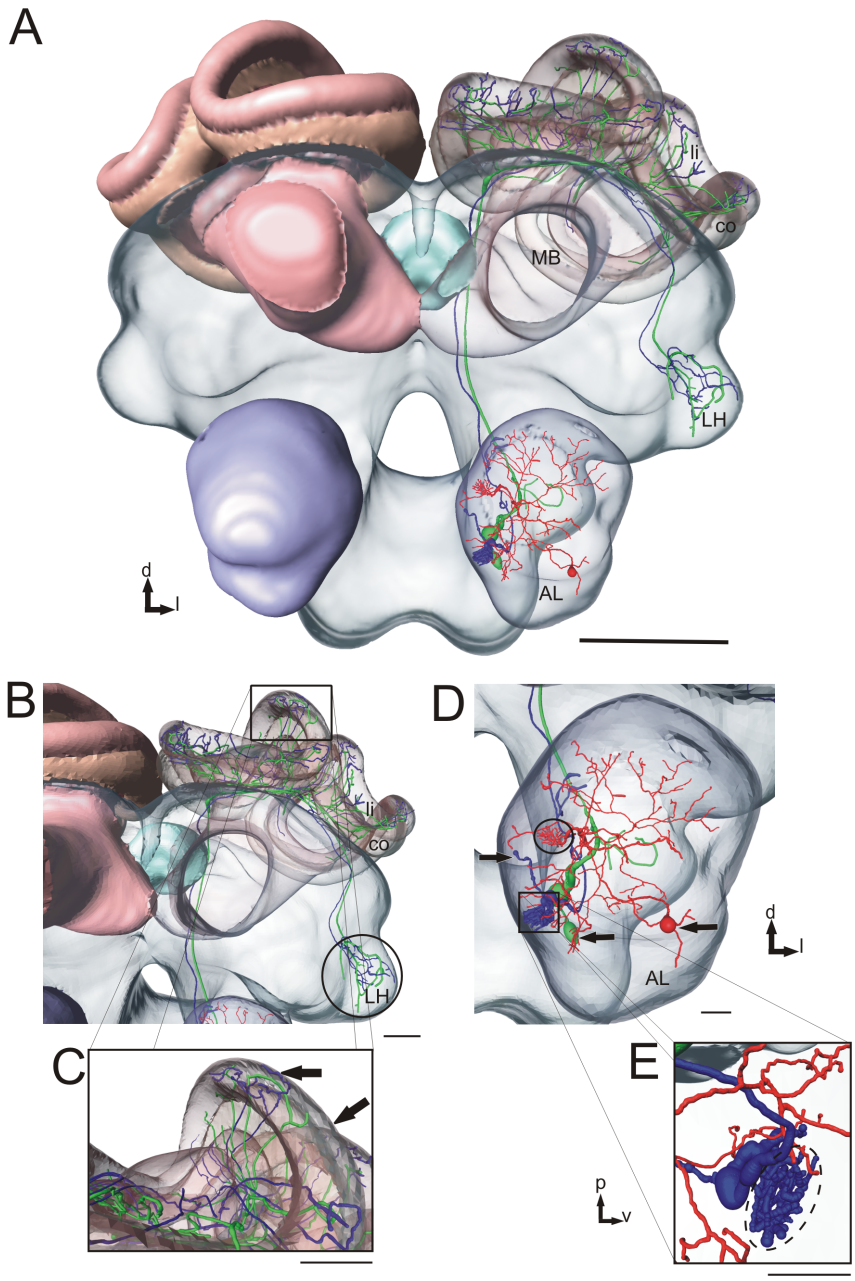

Figure I.5:
Fitting of two projection neurons (PN) and one heterogeneous local interneuron (LI) into the Honeybee Standard Brain (**A**). The uniglomerular PN (type II depicted in blue) arises from the single glomerulus T2-04 (**D**; square). Its soma is located in the medial rind of the antennal lobe (**D**; arrow). The axon leaves the antennal lobe medial-dorsally, runs into the m-ACT, and passes the MB posteriorly, sending collaterals via the inner ring tract to the lip region of the calyces and one collateral to the lateral horn (LH; **B,C**). The uniglomerular PN type II (depicted in green) arborizes from the T3-60 glomerulus. Its soma is located in the ventral rind of the antennal lobe (**D**; arrow). The axon runs in the m-ACT and sends collaterals to the lip region of the calyces (**C**; arrows) and one collateral to the LH (**B**). The heterogeneous LI (depicted in red) shows dense ramifications in the T3-53 glomerulus (**D**; solid circle) and diffusely branches into several other glomeruli. Its soma is located anterior in the ventral cluster (**D**; arrow). The overlap of the PN depicted in blue and the LI within the T2-04 (**E**; dashed circle) glomerulus is shown in D and E (square). For better visualization, the view in **E** is tilted by 90 °C compared with **D**. Scale bars = 200 μm in **A**; 25 μm in **B,D**; 40 μm in **C**; 20 μm in **E**.

the lip. In the PL, there is one collateral for each PN that bypasses the calyces and proceeds ventrally to the LH, where the axon terminals end separately, but in close proximity (circle in Fig. 5B). In a third preparation, a local interneuron (red) of the heterogeneous type (Fonta et al., 1993) has been intracellularly stained and reconstructed. It strongly innervates the T3-53 glomerulus (circle in Fig. 5D) and diffusely branches into several other glomeruli. Figure 5D,E shows the close proximity of the PN (type II, depicted in blue) dendrites and those of the local interneuron within the T2-04 glomerulus. It is shown that the type II PN innervates the core and cortex region of the glomerulus, whereas the local interneuron shows exclusively varicosities in the cortex region (Fig. 5E). The second PN (type I, depicted in green) does not overlap with the local interneuron.

Thus, the structural relationship in 3-D between the local interneuron and the PN can be revealed at high resolution, from reconstruction of the same neurons performed for different brains.

Topography of intrinsic Kenyon cells and extrinsic neurons of the MB The MB are paired neuropils located along the midline in the central brain, each formed by approximately 170,000 intrinsic elements, the Kenyon cells (Kenyon, 1896; Witthoeft, 1967). Their dendritic arborizations give rise to concentrically arranged neuropils that form the medial and lateral calyces. Each calyx is further subdivided into the major compartments of the lip-, collar-, basal ring, and dorsobasal ring neuropils (Rybak and Menzel, 1998; Strausfeld, 2002). Axonal projections of the Kenyon cells originating in the calyces project in bundles into the midbrain, thus forming the peduncle and the vertical and medial lobes of the MB (Strausfeld, 2002); vertical and medial lobes are historically named α- and β-lobes (see, e.g., Howse, 1974; Mobbs, 1982). A major topographical problem with these highly differentiated brain neuropils is the question of how the input zones in the calyces map onto the output regions of the

peduncle-lobe system. Here, we address this issue by comparing a preparation of Kenyon cells (Fig. 4C,D) with a different preparation containing an intracellularly marked extrinsic cell, the PE1, after the cells had been integrated into the Standard Brain (Fig. 6A D). The calyces are organized into modality-specific input layers. The lip and collar neuropils are innervated exclusively by olfactory and visual tracts, respectively. The basal ring and part of the collar receives mixed input from various brain regions, including the subesophageal ganglion (Mobbs, 1982; Menzel et al., 1994; Gronenberg, 2001; Schroeter and Menzel, 2003). This compartmentalized organization of Kenyon cells is maintained within the peduncle and maps onto specific regions of the vertical and medial lobes (Mobbs, 1982). Previous studies have shown that a particular class of clawed Kenyon cells with narrow dendritic fields in all calycal zones (type 5 after Mobbs, 1982, and Rybak and Menzel, 1993; or class II after Strausfeld, 2002) projects to the ventral vertical lobe and the medial lobe. The clawed Kenyon cells disturb the ordered modality-specific projection from the calyces into the lobe system (Mobbs, 1982), and the question arises of whether these Kenyon cell types provide specific input into particular MB extrinsic neurons, e.g., the PE1 neuron as suggested by Strausfeld (2002).

In our study, dye injections into the ventral vertical lobe stained a subset of clawed Kenyon cells (K5) of the medial and lateral calyx (Figs. 4C,D, 6A). The K5 somata are positioned outside the calyx cups [indicated for the median calyx (MC) in Figs. 4C, 6A]. They form narrow dendritic fields at the transition of lip and collar and their axons run within the cup into the proximal peduncle (Fig. 6A). The axon bundle then bifurcates at the transition of the peduncle and the lobes, sending one strand into the medial and the other into the vertical lobe (Figs. 4C, 6A). The PE1 neuron, one of several large protocerebral interneurons, forms a major output pathway from the peduncle to the PL (Mauelshagen, 1993; Rybak and Menzel, 1998). The large tree-shaped dendritic arbors of PE1 project into the peduncle 200 μm below the brain surface at

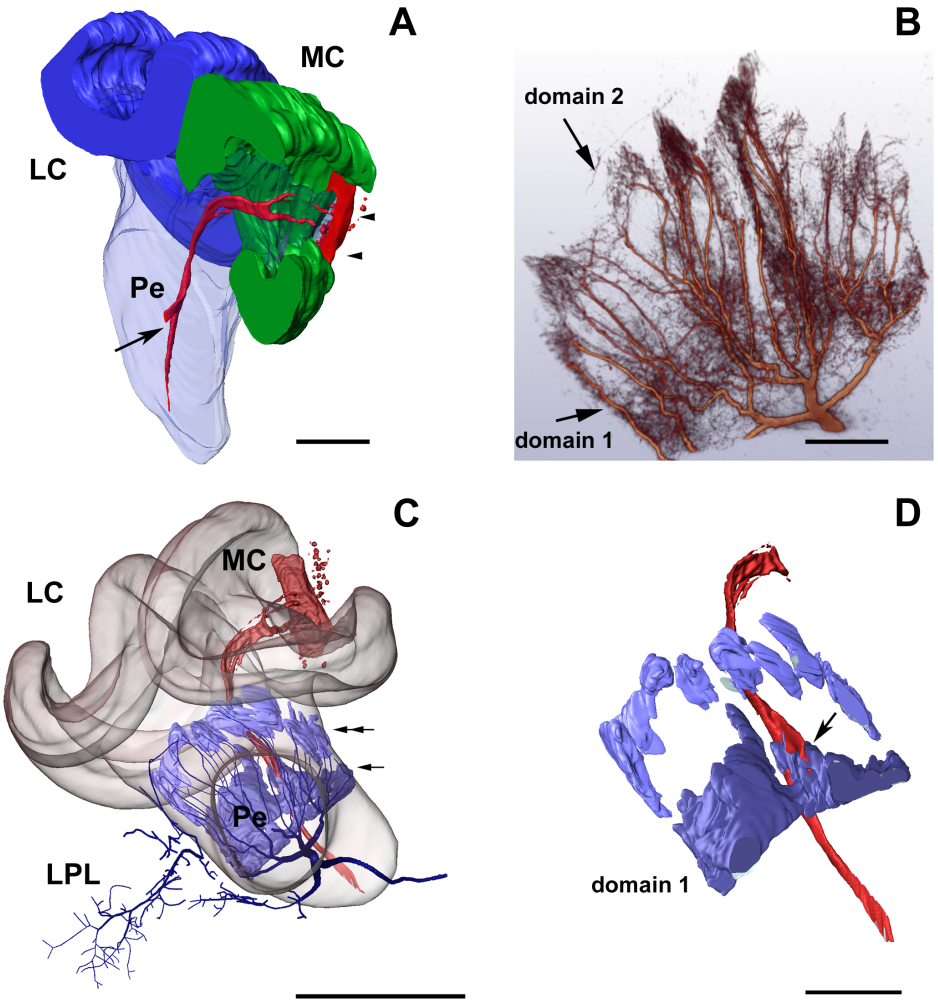

Figure I.6:
A: Passage of Kenyon cell (type 5) axon strands through the calyx and peduncle in the posterior MB. The Kenyon cell axon strands (in red) bifurcate at the transition peduncle and the lobes (arrow). The vertical lobe and the anterior part of the calyces are cut off. K5 somata lie outside the calycal cup in the most posterior protocerebrum (arrowheads, red). At the transition of the lip to collar region of the medial calyx they give rise to fine narrow-field arborizations (in red). **B:** 3-D visualization of dendrites of the PE1 within the mushroom bodies using volume rendering of the original confocal data. Note the dense arborizations in the dendritic tree (domain 1, domain 2). **C:** Combined visualization of Kenyon cells (type 5, shown in red) and PE1 (in blue), from two individuals, registered into the Standard Honeybee Brain. The MB is shown in a transparent view. At the entrance of the MB the large dendritic tree of the PE1 arborizes (visualized here as compact structures; single and double arrows) and extends into the peduncle (Pe). The PE1 exhibits large arborizations in the lateral protocerebral lobe (LPL). **D:** Relative positional information of the PE1 (blue) toward the Kenyon cell bundle (red) in domain 1 is demonstrated. At the bifurcation of vertical to medial lobe, the vertical lobe branch encounters the broad dendritic arborizations of the PE1 (arrow). Scale bars = 100 μm in **A**; 50 μm in **B, D**; 200 μm in **C**.

the base of the vertical lobe. As seen in Figure 6B, fine arborizations of 1 μm in diameter suggest two major dendritic input regions. One (domain 1 in Fig. 6B) is located at the base of the vertical lobe and spans across the lateral extension of the MB. A second one is formed by thin branches that extend dorsoposteriorly approximately 400 500 μm into the peduncle, where they terminate in finger-like structures with dense arborizations, mostly at their tips (domain 2 in Fig. 6B). Because of the location of dendritic arbors, it is concluded that the PE1 neuron receives input from Kenyon cells of all calycal subcompartments, leading to multisensory convergence of Kenyon cells input onto the PE1, a property that was confirmed by intracellular recordings (Mauelshagen, 1993; Rybak and Menzel, 1998). Figure 6C shows the reconstructions of the two preparations semitransparently rendered into the right MB of the standard atlas. For this comparison, the two dendritic domains of PE1 have been reconstructed as closed regions and are depicted in violet. The K5-axon bundle of the medial calyx (red) runs between, and thus bypasses, two most proximal situated dendritic fields of the PE1 ("fingertips" of the PE1, domain 2 in the peduncle). At their bifurcation, the K5 axonal bundle heading into the vertical lobe runs through the broad PE1 dendritic fields (domain 1), whereas the medial lobe strands run medially into the medial lobe, with its most proximal part within the PE1 domain 1 (Fig. 6C,D). This observation was confirmed in other preparations of stained K5 cells (data not shown). In summary, overlapping zones between K5 cells and the PE1 in the peduncle are found at the base of the vertical lobe but not in the finger-like dendritic zones positioned posteriorly in the peduncle.

The Honeybee Standard Brain

For the Honeybee Standard Brain, we raised the average label image resulting from the second nonrigid iteration as reference (see Materials and Methods). This decision was motivated by the fact that the second nonrigid iteration can

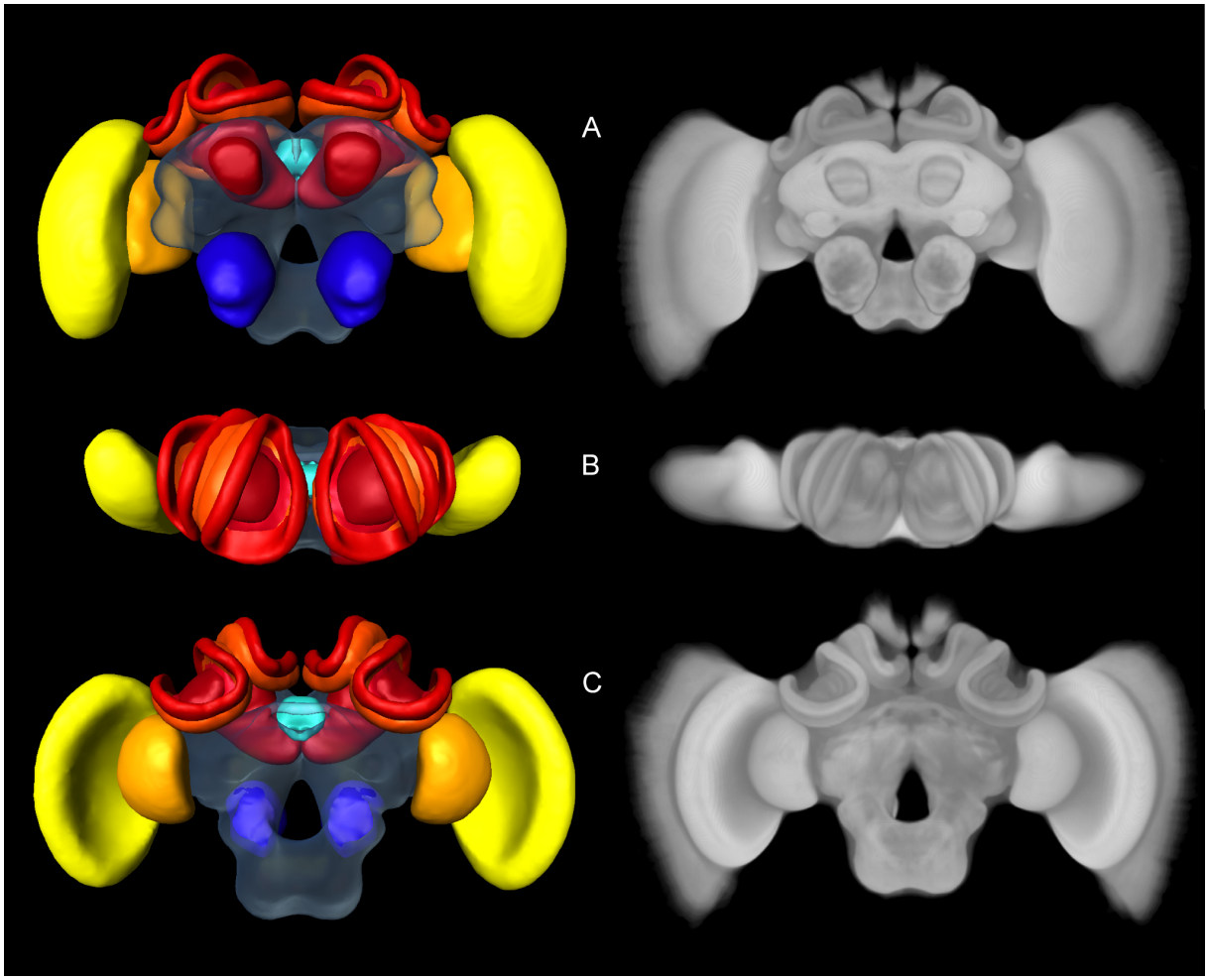

Figure I.7:
The Honeybee Standard Brain. The average label image resulting from the second nonrigid registration iteration was selected as the reference. The left panel shows the surface reconstruction and the right panel is a direct volume rendering of the corresponding average gray image. **A:** Frontal view. **B:** Top view. **C:** Posterior view.

still be seen as an improvement in terms of mapping homologous structures of the individuals (see Fig. 3C). Although the number of undecided voxels still decreases in the following iteration (Table 1), the fine structure details begin to disappear with the third non-rigid iteration. Figure 7 shows different views of the Honeybee Standard Brain. The left panel shows the surface reconstruction, and the right panel is a direct volume rendering of the corresponding average gray image.

Validation of average shape property We shall now validate experimentally the claim that the resulting image has what may be termed an "average shape" property. We operationally defined differences in shape between two brains as the residual nonrigid deformation necessary to map their coordinate systems onto one another after they have been normalized with respect to position and size. Consequently, a property of an average shape brain would be that this residual deformation be minimized. The magnitude of a deformation, D, can be quantified as the sum of all displacement vectors for all foreground voxels of any label image after a 9-DOF affine registration. We compare D for the case in which an individual brain is registered to any of the other individuals with the case in which it is registered to the average. For the average to satisfy the above definition of "averageness", the latter value must be substantially smaller than the former. Figure 8 shows the magnitude of the deformation D in micrometers for any of the 20 brains with respect to the average (marked with diamonds). For comparison, minimum and maximum, as well as the 25^{th} and 75^{th} percentiles, are visualized as box plots for every individual registered to any of the remaining 19 individuals. It is easy to see that the residual deformation, or shape difference, between 19 of the 20 individuals and the average consistently lies in the lower part of the distribution of individual differences. For 12 brains from among 20, the shape difference from the average is even smaller than the minimal D of the difference from any of the remaining individuals. This shows

that our average brain image is indeed a reasonable approximation of a shape centroid of the population, although we may not be able to show whether it is the best such approximation, or even unique.

Discussion

Methodological aspects

Here we present an average shape atlas of the honeybee brain that is based on segmented confocal microscopy images from 20 individuals. We apply this atlas to typical problems in the realm of digital neuroanatomy. We first describe a method for staining the major neuropils by using an immunohistochemical technique. Then, we show how to obtain high-resolution confocal images of the unsectioned honeybee brain. For quantification, the brain images were segmented into 22 morphologically and functionally meaningful regions by interactively tracing them in each of the 20 brain images. In addition to conventional morphometry, which usually consists of extracting properties such as volume and position of the segmented structures, the segmented brain images can be used to extract shape information that is common to all of the subjects. In contrast to similar approaches aimed at generating population-based atlases (Ashburner, 2000; Guimond et al., 2000), we apply a method here that takes the segmented images instead of the original microscopy images. The reason for this is mainly technical: the immunostainings of the whole-mount brain preparations are very nonhomogeneous and, therefore, difficult to process directly with the intensity-based registration algorithm. The resulting average image can be termed a "shape centroid" of the subject population in the sense that the deformation of any individual image necessary to match the average is smaller than the mean intersubject deformation. We have verified this property quantitatively (Fig. 8). By minimizing the shape difference between the Standard Brain and any given individual, the average shape atlas has a couple of advantages over a standard

chosen as the "most typical" individual. First, when the Standard Brain is used to integrate structural data coming from different individuals, the average-shape property ensures that the deformation applied to the individuals remains small. Second, manual segmentation is subject to noise, i.e., contouring between slices varies according to criterion variability of the experimenter. Averaging several such noisy label images reduces random parts of the contours, thus increasing the reliability of the standard.

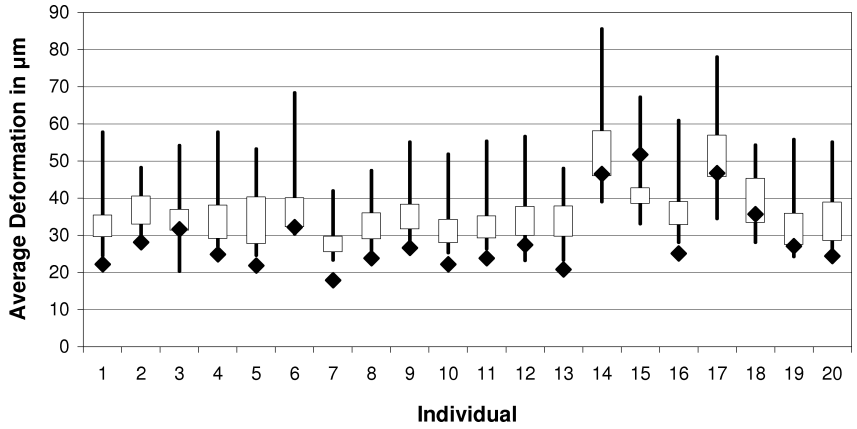

Figure I.8:
Comparison of the shape differences between each individual brain image (numbered 1 20) and the average (diamonds) with that between the individual and the remaining 19 brains (boxes and whiskers), showing minimum and maximum as well as 25^th and 75^th percentiles. The shape difference is quantified by averaging the displacements (in micrometers) of all foreground voxels. The shape difference between 19 of the 20 individuals and the average lies in the lower part of the distribution of differences to all individuals. For 12 brains the shape difference to the average is even smaller than the minimal deformation D of the difference to the remaining individuals.

Comparison with the *Drosophila* Standard Brain

The *Drosophila* Standard Brain (Rein et al., 2002) is very closely related to the bee brain atlas. As with the honeybee, a population of whole-mount Drosophila brains stained with a generic neuropil marker was imaged with the confocal microscope and segmented into various brain regions. Subsequently, images were transformed into the same affine space to allow the computation of average intensity and probability maps. Unlike the case with the honeybee, the transformations were restricted to rigid or rigid-plus-isotropic scaling. Furthermore, the

authors also propose a nonrigid method, in which (after global rigid registration) each substructure is individually aligned by using rigid registration. No attempt was made to extract an average-shape image. Instead, a representative individual was presented that was defined as the label image closest to the average label image. Generally, the *Drosophila* approach seems quantitatively more rigorous: If one is to quantify differences with respect to size, then registrationincluding scaling would eliminate such differences. The same argument holds for nonrigid deformations: because such algorithms are designed to minimize differences with respect to shape, those differences will no longer be visible. Besides that, in intersubject nonrigid registration, there is no meaningful way to determine whether the algorithm actually finds anatomically corresponding parts in each image. It is not even known whether (and in fact seems very unlikely that) there is a one-to-one correspondence between different subjects on all levels of spatial scale. Still, with the Honeybee Standard Brain, we are using an approach that includes nonrigid registration. The reasons for this are discussed in the following paragraphs. First, the primary application of the Standard Brain is as a spatial reference frame for the interindividual comparison of structural and functional data. Because shape variability was quite considerable, an average brain atlas computed after rigid registration would have exhibited artifacts such as holes in small structures. This is due to the fact that small structures at the periphery of the brain, such as the calyx subcompartments, will most likely not overlap after rigid or affine registration. Also, for similar reasons, the relative size of structures will not be preserved after rigid alignment. Second, average gray images generated after rigid or affine registration lack, in our view, any biological meaning. Obviously, it does not make sense to average gray values originating, for example, from basal ring of one individual and the collar neuropils of another. Essentially such averages give us a visual impression of the shape variability of the population. Nevertheless, we are aware of the fact that the registration algorithms used in this study are limited in their ability to

map any given individual image accurately onto the fixed reference image everywhere in the image. However, as shown by the sequence of average gray images calculated from the transformed label images (cf. Fig. 2) the nonrigid registration is able to increase the distinctness of inner structures such as tracts and strata even though the algorithm does not "know" about those structures, because it is applied on the structureless label images. Therefore, we believe that registration fidelity is sufficient for the spatial scale level of the Standard Brain. Finally, this result also makes us optimistic that a nonrigid registration of neuropil boundaries to the standard yields a reliable and reasonably accurate estimate of the "true" position of a costained neuron in that standard.

Tissue shrinking

To visualize the immunohistochemically treated brain, the preparations had to be dehydrated and cleared in MS. Besides fixation, this treatment is known to introduce considerable amounts of tissue shrinking (Bucher et al., 2000). Hence, the standard as presented here refers to a fixed, dehydrated, and cleared brain rather than to the in vivo situation. This is a limitation only in those cases in which the Standard Brain is to be used as a stereotactic reference for in vivo experiments. However, for the purpose of integrating structural data such as single-cell reconstructions into the standard, this might not be a severe limitation as long as the preparations undergo similar histological treatment, leading to similar spatial distortions of the specimen. Because tissue dehydration and clearing are essential for confocal imaging of the bee brain, the standard as presented here will fit the needs of structural bee anatomy.

Compiling single marked neurons from different brains

Brains are made up of neurons. Neurons, again, form anatomically and functionally defined circuits. Insect brains contain a large number of individually

identifiable neurons whose connectivity is still poorly understood. Although marking tracts, i.e., bundles of neuron axons, with multiple dyes may reveal convergence regions and indicate potential connectivity (Gronenberg and Hoelldobler, 2001; Gronenberg, 2001; Schroeter and Menzel, 2003; Evers et al., 2005), the combination of physiological and anatomical studies at the level of single, identified neurons provides a unique opportunity to relate anatomical to functional connectivity. The very problem of such endeavors is that experiments have to be carried out in multiple individuals, with each preparation providing information on a single neuron only. The Standard Brain can help to solve this problem. Because it is average in shape, a nonrigid registration that is necessary to minimize shape differences across individual brains is facilitated, thus allowing the covisualization of reconstructed neurons within a common frame. The applications presented in this study show that this strategy is useful and provides important new insights. At the AL level, the branching patterns of LIN and PN can be assigned to the appropriate glomeruli, the latter serving as functional units in the first stage of olfactory processing. A thorough map of olfactory interneurons therefore nicely complements physiological data from Caimaging experiments on the function of the glomeruli (Joerges et al., 1997; Galizia and Menzel, 2000). In addition, it is feasible to analyze the spatial relations between a single uniglomerular PN (type II) and an LIN within the corresponding glomerulus. Figure 5D shows the spatial properties of neuronal wiring within the T2-04 glomerulus. The fact that the type II PN densely innervates the core and cortex region of the T2-04 glomerulus, whereas the LIN sends only one branch into the cortical layer of this glomerulus, leads to the question of whether, in this case, this cortical layer of the glomeruli is specific for the potentially synaptic contact between receptor cells and LIN. Ganeshina and Menzel (2001) described the patterns of blebs in axodendrons of PNs in the secondary olfactory neuropil, the MB. The terminals of the two m-ACT neurons described in our study (Fig. 5) can be embedded into their common

target region (the MBs lip neuropil) within the Standard Brain atlas, thus identifying the structural correlates of olfactory coding at the level of the input side of the MB. A similar topic can be addressed for the LH. In Figure 5A,B, we demonstrate that two m-ACT PNs exhibit overlapping branching patterns in the MB lip region and the LH. The lack of axonal ACT terminals in some areas is due to noninnervation of the lip neuropil (see also Abel et al., 2001); additional data will allow us to prove whether particular regions and / or strata in the MB lip are served by particular ACT neurons. A challenging task in insect neuroanatomy has been determining the topography of the MB and its connectivity to extrinsic neurons at the calycal input and the peduncle lobe output regions (Mobbs, 1982; Rybak and Menzel, 1993; Gronenberg, 2001; Strausfeld, 2002). In this study, for the first time, the close spatial proximity between a specific subset of Kenyon cell axons (clawed Kenyon cells) and an identified extrinsic neuron within the peduncle of the MB, the PE1 cell, is demonstrated by using two preparations (Figs. 4, 6). A general problem of neuron reconstructions has been addressed in this context and solved with the help of the standard atlas. High-resolution imaging requires objectives whose working distance is often not large enough to cover the whole dendritic tree of the respective neuron, in our case the PE1 neuron. Vibratome sections are the solutions to this problem, but consecutive sections have to be aligned such that the neuron can be fully reconstructed and registered into the atlas. Here the standard atlas provides the frame for precise alignment if, as in our case, the neuropil borders were segmented and used as local landmarks for the registration process. The physiology of PE1 has been characterized previously (Mauelshagen, 1993; Rybak and Menzel, 1998). Its responses are multimodal, and it changes its response properties to olfactory stimuli when the animal is sensitized or conditioned to an odor. The question arises of whether and how a multisensory integrating neuron such as PE1 may both serve the function of reading out specific (e.g., olfactory) memory and at the same time respond to a large variety of stimuli.

In the MB, most Kenyon cells map from radial organized zones in the calyces onto the linearly arranged peduncle and lobe systems. In addition, Kenyon cells from a particular class (clawed Kenyon cells, type 5) do not follow the regular projection pattern of the other Kenyon cells and converge instead into the ventral vertical lobe (Rybak and Menzel, 1993; Strausfeld, 2002). In the tree-shaped dendritic branching of PE1, two major input zones can be distinguished, characterized by fine arbors smaller than 1 μm in diameter (Fig. 6B). Domain 1 is located at the base of the vertical lobe and domain 2 in the finger-like zones of the posterior peduncle. Here we show that K5 axons contact the PE1 at the base of the vertical lobe, where PE1 forms broad dendritic fields, but the K5 axons do not impinge onto domain 2 (Fig. 6D). However, clawed Kenyon cells are certainly not the only input to the PE1; Kenyon cells with somata inside the calycal cup and arborizations in the lip, collar, or basal ring (class KI, after Strausfeld, 2002) cross the finger-like domains of PE1 (domain 2). In this region, Kenyon cells have been proved to form output synapses onto the PE1 (Rybak and Mauelshagen, 1994). We therefore conclude that the PE1 receives input from most Kenyon cells and not only from a subsystem (clawed Kenyon cells) as suggested by Strausfeld (2002). This neuroanatomical finding is consistent with the multisensory properties of PE1 (Mauelshagen, 1993; Rybak and Menzel, 1998; Iwama and Shibuya, 1998). Moreover, the ventral vertical lobe might therefore integrate sensory information from different modalities via the clawed Kenyon cells, a view further substantiated by Strausfeld (2002).

Conclusion

The Honeybee Standard Brain represents a valuable new tool for compiling structural data from across individuals in a single, joint representation. Here we show 1) that dendrites of m-ACT neurons branch in the whole glomerulus of the AL and overlap with dendrites of local interneurons in the cortical layer; 2) that

axon terminals of different m-ACT neurons arborize in separate areas in both the lip neuropil of the MB and in the LH; 3) that clawed Kenyon cells, a subclass of intrinsic MB neurons, project to both lobes of the MB and contact the proximal dendritic tree of the MB-extrinsic PE1; and 4) that the PE1 neurons receive input not only from the clawed Kenyon cells but also in a different region of its dendritic tree from Kenyon cells across the peduncle. These results show that the Honeybee Standard Brain can be successfully and efficiently used to solve questions regarding the structural basis of neural circuits at the single-cell level with high precision. In future work, anatomical data will also be cross-linked with functional measures, resulting in an ever-growing multimodal database. Resolution and size of the current atlas have been chosen to cover the gross anatomy of the honeybee brain. If necessary, however, images can be sampled at higher spatial frequencies if the structure in question does not lie too deep in the brain or if the brain is sliced. Partial images can then be aligned with the Standard Brain to provide a large amount of additional information for particular parts of the brain or parts of neurons or neuropils. Nonfluorescent preparations derived from in situ hybridization, or classical stains (e.g., Golgi stains), can in principle be included into the Standard Brain data set. Reaching electron microscopic (EM) resolutions and including localized and aligned EM sections are also conceivable but have not yet been achieved. On the other end of the spatial resolution scale, one might want to correct the structural distortions induced by the histological procedures (dehydration and clearing) and relate the Standard Brain or an individual brain to the in vivo situation. This could be achieved by nonrigid registration procedures applied to the virtual model as derived from optical sectioning to match the images as measured with high-resolution magnetic resonance imaging (Haddad et al., 2004).